The Astrophysical Journal, 835:244 (11pp), 2017 February 1 doi:10.3847/1538-4357/835/2/244

Fan Loops Observed by *IRIS*, EIS, and AIA

Avyarthana Ghosh[1,2], Durgesh Tripathi[1], G. R. Gupta[1], Vanessa Polito[3], Helen E. Mason[3], and Sami K. Solanki[4,5]
[1] Inter-University Centre for Astronomy and Astrophysics, Post Bag—4, Ganeshkhind, Pune 411007, India; avyarthana@iucaa.in
[2] Center of Excellence in Space Sciences India, Indian Institute of Science Education and Research, Kolkata, West Bengal 741246, India
[3] Department of Applied Mathematics and Theoretical Physics, Wilberforce Road, Cambridge CB3 0WA, UK
[4] Max-Planck Institute for Solar System Research, Justus-von-Liebig-Weg 3, D-37077 Göttingen, Germany
[5] School of Space Research, Kyung Hee University, Yongin, Gyeonggi-Do, 446-701, Korea
Received 2016 July 10; revised 2016 December 16; accepted 2017 January 5; published 2017 February 1

Abstract

A comprehensive study of the physical parameters of active region fan loops is presented using the observations recorded with the *Interface Region Imaging Spectrometer* (*IRIS*), the EUV Imaging Spectrometer (EIS) on board Hinode, and the Atmospheric Imaging Assembly (AIA) and the Helioseismic and Magnetic Imager (HMI) on board the *Solar Dynamics Observatory* (*SDO*). The fan loops emerging from non-flaring AR 11899 (near the disk center) on 2013 November 19 are clearly discernible in AIA 171 Å images and in those obtained in Fe VIII and Si VII images using EIS. Our measurements of electron densities reveal that the footpoints of these loops are at an approximately constant pressure with electron densities of $\log N_e = 10.1\,\mathrm{cm}^{-3}$ at $\log [T/K] = 5.15$ (O IV), and $\log N_e = 8.9\,\mathrm{cm}^{-3}$ at $\log [T/K] = 6.15$ (Si X). The electron temperature diagnosed across the fan loops by means of EM-Loci suggest that two temperature components exist at $\log [T/K] = 4.95$ and 5.95 at the footpoints. These components are picked up by *IRIS* lines and EIS lines, respectively. At higher heights, the loops are nearly isothermal at $\log [T/K] = 5.95$, which remained constant along the loop. The measurement of the Doppler shift using *IRIS* lines suggests that the plasma at the footpoints of these loops is predominantly redshifted by 2–3 km s^{-1} in C II, 10–15 km s^{-1} in Si IV, and 15–20 km s^{-1} in O IV, reflecting the increase in the speed of downflows with increasing temperature from $\log [T/K] = 4.40$ to 5.15. These observations can be explained by low-frequency nanoflares or impulsive heating, and provide further important constraints on the modeling of the dynamics of fan loops.

Key words: Sun: activity – Sun: chromosphere – Sun: corona – Sun: magnetic fields – Sun: transition region – Sun: UV radiation

1. Introduction

The observations from modern high-resolution instruments reveal that active regions comprise a variety of loop structures. These loops are considered to be the building blocks of the solar corona. Therefore, a comprehensive understanding of the physics of all types of loops is key to the problem of solar coronal heating (see Klimchuk 2006; Reale 2014; De Moortel & Browning 2015; Klimchuk 2015, for reviews).

Active region loops are broadly classified into three categories—namely, hot core loops (3–5 MK), warm loops (1–2 MK), and fan loops (0.6–1 MK). In addition, there is a significant amount of diffuse plasma spread over a large area at coronal temperatures without any well-defined visible structures, possibly because we currently lack instruments with sufficiently high spatial resolution (Del Zanna & Mason 2003; Viall & Klimchuk 2011; Subramanian et al. 2014).

The hot loops are rooted in moss regions (Berger et al. 1999; Antiochos et al. 2003; Tripathi et al. 2010, 2012) and have electron densities $\log N_e = 9.58\,\mathrm{cm}^{-3}$ and $9.26\,\mathrm{cm}^{-3}$ for Fe XIV ($\log [T/K] = 6.30$) and Fe XIII ($\log [T/K] = 6.25$), respectively (Brosius et al. 1997; Tripathi et al. 2010; Del Zanna 2013). The observations of hot loops reveal that a range of frequencies of heating events may be present in the core of active regions (Tripathi et al. 2011; Warren et al. 2011a, 2012; Del Zanna et al. 2015). Warm loops are believed to be multi-stranded structures with electron densities ranging between $\log N_e = 8.5$ to $9.0\,\mathrm{cm}^{-3}$. Their properties can be explained by low-frequency impulsive heating (see, e.g., Del Zanna & Mason 2003; Warren et al. 2003; Klimchuk 2006; Tripathi et al. 2009; Ugarte-Urra et al. 2009; Gupta et al. 2015).

Fan loops may be the most complex and longest living loop structures. They form at the periphery of active regions and were first studied in detail by Schrijver et al. (1999) using the observations recorded by the Transition Region and Coronal Explorer (TRACE; Handy et al. 1999). Fan loops are thought to be rooted in the penumbrae of sunspots, in close proximity to active regions with relatively strong magnetic fields, in enhanced network zones, or even in unipolar quiet-Sun network regions. These structures connect regions of high flux concentrations across distances as large as 10^5 km or more (Schrijver et al. 1999). While their lifetimes typically range from several hours to days, the evolution timescale is a fraction of an hour (Schrijver et al. 1999).

One of the earliest spectroscopic studies of fan loops was performed by Winebarger et al. (2002) using observations made with the Solar Ultraviolet Measurements of Emitted Radiation (SUMER; Wilhelm et al. 1995) on board the *Solar and Heliospheric Observatory* (SoHO). These fan loops were observed in the emission line of Ne VIII 770 Å ($\log [T/K] = 5.80$), and the plasma in these loops showed persistent downflows (redshifts) of 15–40 km s^{-1}. We note, however, that the reference wavelength used to derive the Doppler shift was 770.409 Å, and this was revised to 770.428 ± 0.007 Å by Peter & Judge (1999) and to 770.428 ± 0.003 Å by Dammasch et al. (1999) using SUMER observations. The use of the revised wavelength will therefore reduce the Doppler shift in fan loops that was computed by

Winebarger et al. (2002) by ~5–10 km s^{-1}. Based on hydrodynamic modeling, the observed flows were attributed to nonuniform asymmetric heating of the loops. Later on, Marsch et al. (2004) studied fan loops observed over three active regions and found Doppler velocities of ~±5 km s^{-1} for H I Lyβ 1025 Å ($\log[T/K] = 4.00$) and ~±2 km s^{-1} for Si II 1533 Å ($\log[T/K] = 4.20$). At higher temperatures, the redshifts increased to ~5 km s^{-1} in C IV 1548 Å ($\log[T/K] = 5.05$), and ~15–20 km s^{-1} in the spectral lines of both N V 1548 Å and O VI 1031 Å formed at $\log[T/K] = 5.30$ and 5.45, respectively. However, the redshift decreased to ~10 km s^{-1} in the spectral line of Ne VIII 770 Å. Still more recently, Doschek (2006) reported that the plasma flowing along the field lines in these fan loops was blueshifted by 5–10 km s^{-1} in Ne VIII 770 Å and S V 786 Å ($\log[T/K] = 5.20$) lines.

With the launch of the EUV Imaging Spectrometer (EIS; Culhane et al. 2007) on board Hinode, the measurements of physical parameters such as electron densities, temperatures, and Doppler shifts in various structures within a temperature span from the upper transition region to the corona have been performed routinely (see e.g., Del Zanna 2008; Doschek et al. 2008; Mariska et al. 2008; Tripathi et al. 2009, 2012; Dadashi et al. 2012; Winebarger et al. 2013). Doppler shifts of the plasma confined in fan loops were measured using EIS observations by Warren et al. (2011b) and Young et al. (2012). Warren et al. (2011b) showed that the plasma at the footpoints of fan loops was redshifted by ~30 km s^{-1} in Si VII ($\log[T/K] = 5.80$) line and also suggested, based on magnetic field extrapolation, that fan loops are closed loop structures, although the other footpoints may not be visible in coronal images. Young et al. (2012) reported that plasma in the fan loops was redshifted (~15–20 km s^{-1}) in Fe VIII line at $\log[T/K] = 5.80$, but were blueshifted (~25 km s^{-1}) in the emission lines of Fe XII (above $\log[T/K] = 6.20$) at their footpoints. At intermediate temperatures (Fe X line, $\log[T/K] = 6.00$), they observed mixed signatures of downflows and upflows.

The *Interface Region Imaging Spectrograph* (*IRIS*; De Pontieu et al. 2014), which was launched in 2013, provides a remarkable opportunity to study the various physical plasma parameters in the solar atmosphere all the way from the chromosphere to the corona when it is combined with the EIS. In this paper, we study a set of fan loops emanating from a sunspot using simultaneous observations recorded by *IRIS*, EIS, the Atmospheric Imaging Assembly (AIA; Lemen et al. 2012), and the Helioseismic and Magnetic Imager (HMI; Schou et al. 2012a, 2012b) on board the *Solar Dynamics Observatory* (*SDO*; Pesnell et al. 2012). The rest of the paper is structured as follows. In Section 2 we provide a brief description of the instruments we used and discuss the processing techniques. Analysis and results are presented in Section 3, followed by a summary and discussion of the results in Section 4.

2. Observations

The analyzed active region (*AR 11899*) appeared on the east limb of the Sun on 2013 November 12 and was observed at heliographic coordinates of 284W, 31N on 2013 November 19. On this date, this active region was observed nearly simultaneously by Hinode/EIS, *IRIS*, *SDO*/AIA, and HMI. Figure 1(A) displays the full-disk AIA image taken with the 171 Å channel. The overplotted black box is the EIS raster field of view (FOV) for CCD B, the blue box is the *IRIS* slit-jaw image (SJI) FOV, and the green box is the *IRIS* raster FOV. The red box in Figure 1(A) is the region highlighted in Figure 1(B) showing the fan loops in detail. The EIS raster images of the active region using two emission lines (Si VII 275.35 Å at $\log[T/K] = 5.80$ and Fe XII 195.12 Å at $\log[T/K] = 6.20$) are plotted in Figures 1(C) and (D). The maps in Figures 1(B), (C), and (D) are plotted using a negative-intensity scale. The gaps in Figures 1(C) and (D) between $x = [228'', 292'']$ are caused by missing data in the EIS raster. Henceforth, this region has been neglected in our analysis. The blue and green boxes on these EIS intensity maps show the FOV of *IRIS* SJI and raster, respectively. However, in all the later figures, the *IRIS* raster FOV has been reduced so as to focus on the footpoint region alone.

To determine the plasma densities and temperatures in the fan loops, spectroscopic data from *IRIS* and EIS were used. For Doppler velocities, however, only *IRIS* observations were used. For this particular observation, EIS used the 2″ slit to raster over 150 positions (i.e., time steps) between 10:40:20 UT and 11:59:00 UT with an exposure of ~30 s so that the EIS FOV is [300″, 300″]. *IRIS* rastered a FOV of [20″, 182″] six times over a period of ~32 minutes (between 10:31:15 UT and 11:03:31 UT). Each raster is 5 minutes and 17 s long. The spectral lines from *IRIS* and EIS that we used for this study are listed in Table 1, along with their laboratory wavelengths taken from Sandlin et al. (1986) for *IRIS* lines and from Brown et al. (2008) for EIS lines. Note that the reference wavelength for Si VII mentioned in Brown et al. (2008) should be corrected to 275.368 Å (see Warren et al. 2011b). The peak formation temperatures have been taken from CHIANTI (Dere et al. 1996; Landi et al. 2013).

In this study we used level-2 data from *IRIS* and level-0 data from EIS. The *IRIS* data are corrected for all instrumental effects such as flat-fielding, dark currents, and offsets to make them suitable for all scientific purposes[6], including thermal orbit variations. During the length of each raster of 5 minutes 17 s, the orbital error is also expected to be negligible. However, we estimated the residual orbital variations for a single raster as well as over the entire duration of the six rasters and concluded that it is negligible. The *IRIS* data are analyzed using Gaussian fitting routines provided in solarsoft.[7] EIS level-0 data were preprocessed with the eis_prep.pro[8] routine. For the wavelength calibration, orbital drift and slit tilt errors are two major sources of concern. The eis_auto_fit.pro routine[9] rectifies the EIS spectral data by removing these errors.

In this study we have data in two *IRIS* spectral windows, namely C II and Si IV. Within the C II window there are two C II lines at 1334.5 Å and 1335.71 Å ($\log[T/K] = 4.40$), but the signal strength is poor for both of them. Hence, a 4 × 4 pixel binning is performed. The Si IV window harbors two lines at 1394.78 Å and 1402.77 Å ($\log[T/K] = 4.90$). The Si IV window centered at 1402.77 Å also has two O IV lines observed at 1399.77 Å and 1401.16 Å ($\log[T/K] = 5.15$). For the O IV lines, a 4 × 4 pixel binning is required because of the poor signal-to-noise ratio (S/N). These two lines of O IV are density

[6] A Users Guide To *IRIS* Data Retrieval, Reduction and Analysis, S.W. McIntosh, 2014 February.
[7] Using EIS Gaussian fitting routines for *IRIS* data, P. Young, 2014 April.
[8] EIS Software Note No. 13, P. Young, 2010.
[9] EIS Software Note No. 16, P. Young, 2015.

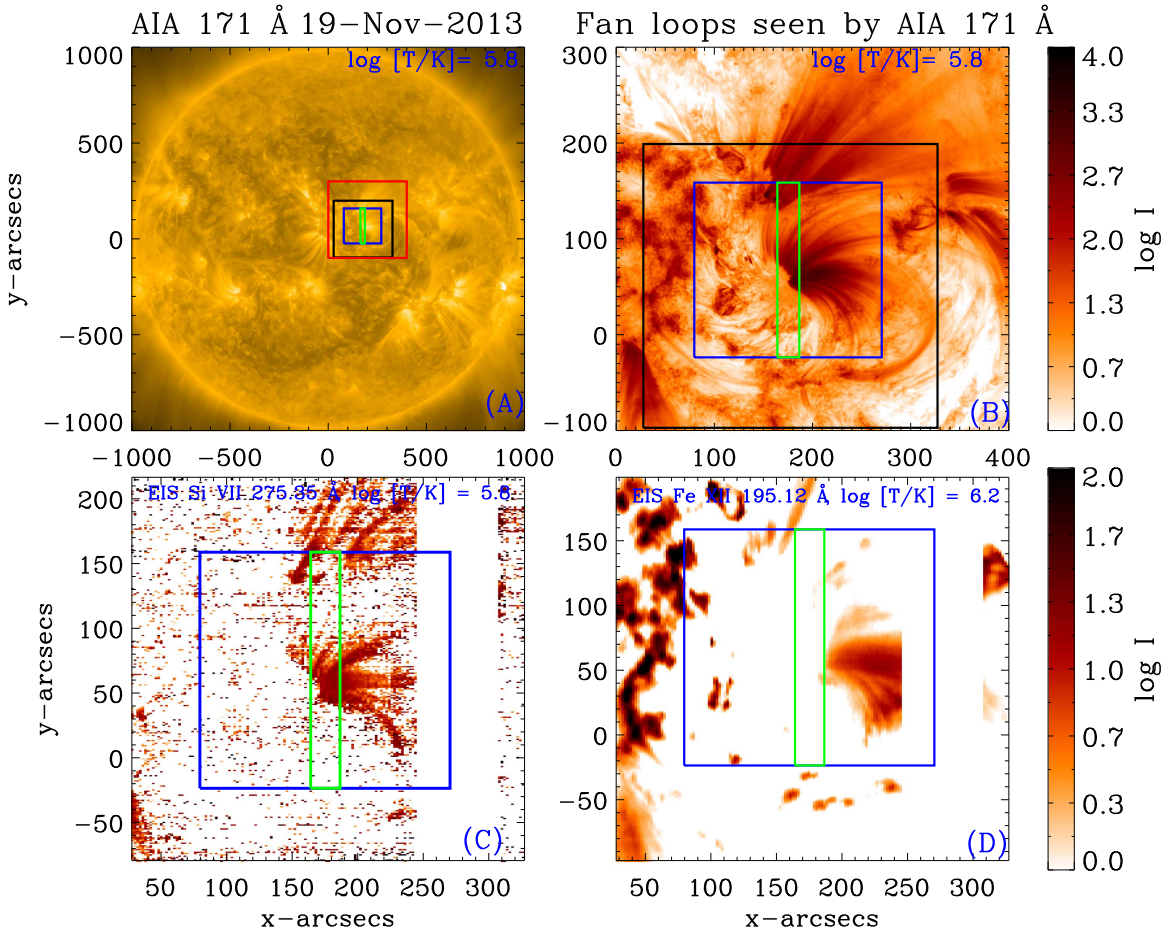

Figure 1. (A): full-disk AIA image at 171 Å showing AR 11899, recorded on 2013 November 19 at 10:39:59 UT. The overplotted red box is the AIA FOV zoomed in in panel (B). (B): AIA 171 Å image (in negative-brightness scale) showing the fan loops. (C): EIS Si VII 275.35 Å raster image (in negative-brightness scale) showing the fan loops between 10:40:20 UT and 11:59:00 UT. (D): EIS raster image of the same region in the Fe XII 195.12 Å line (in negative-brightness scale). In (A) and (B), the black box is the EIS raster FOV (CCD B). In all four panels, the superimposed blue and green boxes represent the *IRIS* slit-jaw image (SJI) and *IRIS* raster FOV at 10:36:39 UT, respectively.

sensitive and are used for the measurement of electron densities under the assumption of a Maxwellian distribution of electron velocities (see, however, Dudík et al. 2011).

For the EIS spectral analysis (see Table 1), we use lines from Fe VIII (log $[T/K] = 5.65$) to Fe XIV (log $[T/K] = 6.30$). The Fe VIII 194.66 Å line is blended in its red wing, at 194.80 Å (Young et al. 2007), which is removed using a double Gaussian fit. The Fe XII line at 195.12 Å has a self-blend at 195.18 Å, but its contribution is negligible (<10%) in regions with densities lower than log $N_e = 9.5\,\mathrm{cm}^{-3}$ at log $[T/K] = 6.20$. Therefore, fitting a single Gaussian suffices.

One important aspect of measuring the Doppler shifts is to determine a reference wavelength. Generally, neutral or singly ionized photospheric or chromospheric lines serve the purpose of determining the in-flight absolute wavelength drift (Hassler et al. 1991) when there are no calibration lamps on board.[10] *IRIS* has an S I line with a rest wavelength of 1401.5136 Å (De Pontieu et al. 2014). The observed wavelength of the same S I line is 1401.52 Å (averaged over the entire raster), which translates into a velocity difference of $\sim$1.0 km s^{-1}. This line is used for the absolute wavelength calibration of all *IRIS* lines. For the EIS instrument, however, there are no neutral spectral lines or on-board calibration lamps. A method to obtain absolute velocities from EIS was derived by Young et al. (2012). This uses the quiet-Sun region in the Fe VIII line to obtain the reference wavelength. Unfortunately, no such region could be identified in our observations. We therefore did not attempt to derive Doppler velocities using EIS lines.

Our aim is to study the various physical parameters of the plasma within the fan loops using *IRIS* and EIS. Therefore, we need to coalign the EIS and *IRIS* images. Since AIA gives full-disk images at different temperatures, these can be used as references to coalign the *IRIS* and EIS observations. For this purpose, we first overplot the *IRIS* raster obtained in Si IV 1402.77 Å (plotted in contours in Figure 2(A)) on an *IRIS* SJI taken in Si IV 1400 Å (the reference image in (Figure 2(A))) to check for any misalignment. The Si IV SJI is then coaligned with 1600 Å images taken by AIA (Figure 2(B)). This is followed by coaligned images of AIA 171 Å channel on *IRIS* Si IV 1400 Å SJI (Figure 2(C))) in the background. Furthermore, the AIA 171 Å channel image is coaligned with AIA 1600 Å image. The raster image obtained in EIS Fe VIII was coaligned with AIA images taken at 171 Å. Figure 2 displays the coaligned *IRIS*, EIS, and AIA images.

[10] *IRIS* Technical Note 20: Wavelength Calibration, 2013 January 9.

Table 1
IRIS and EIS Spectral Lines Used for Studying the Fan Loops Emanating out of AR 11899 on 2013 November 19, where λ_0 is the Rest Wavelength

IRIS Lines			EIS Lines		
Ion name	λ_0 (Sandlin et al. 1986) (Å)	Peak formation temperature (log) (T/K)	Ion name	λ_0 (Brown et al. 2008) (Å)	Peak formation temperature (log)(T/K)
C II	1334.532	4.40	Fe VIII	194.663	5.65
C II	1335.708	4.40	Si VII	275.368 (Warren et al. 2011b)	5.80
Si IV	1393.755	4.90	Si X[a]	258.375	6.15
Si IV	1402.770	4.90	Si X[a]	261.058	6.15
O IV[a]	1399.755	5.15	Fe XII	195.119	6.20
O IV[a]	1401.156	5.15	Fe XIII	202.044	6.25
			Fe XIV	264.787	6.30

Note. The peak formation temperatures are taken from CHIANTI (Dere et al. 1996; Landi et al. 2013) at one particular density.
[a] Density-sensitive line pair.

3. Data Analysis and Results

In Figure 3 the 1600 Å and 1700 Å images correspond to the near-continuum. They show the sunspot umbra fringed by the penumbra and a scattered bright plage. The 304 Å channel primarily corresponds to the emission in the He II line that shows the sunspot (which does not appear dark in this channel) and the active region in the hottest part of the chromosphere ($\log[T/K] = 4.70$). The images in the second and third rows of the Figures 3(D)–(H) display the morphology of the fan loops emanating from the sunspot at different characteristic temperatures. Figure 3(I) shows the line of sight (LOS) magnetogram. The magnetogram clearly indicates a bright region, corresponding to an apparent opposite-polarity field within the sunspot umbra, although this may well be a location of anomalous polarization rather than a true opposite polarity.

As can be seen in Figure 3, the fan loops are seen in almost all the channels of AIA. This is essentially because all the channels have some contribution from low-temperature lines forming below a million degrees (see, e.g., O'Dwyer et al. 2010, for more detail). The fan loops are most prominent in the image taken in the AIA 171 Å channel at $\log[T/K] = 5.80$. As the temperature rises further, the loops become less and less perceptible. A similar effect was observed for the warm loops by Tripathi et al. (2009), and it was modeled by Guarrasi et al. (2010). However, the 131 Å channel of AIA has a significant contribution from the Fe VIII line that formed at $\log[T/K] = 5.60$. This Fe VIII line emission appears as the very bright loops emanating from the footpoint region even in the 131 Å channel. The 94 Å channel has contributions from several transitions of Fe X and Fe XIV formed across a wide temperature range (Del Zanna et al. 2012). The intermediate-temperature channels, 193 and 211 Å, show gradual fading of the loops in the background, whereas the cores are still visible. Examining the intensity maps obtained using EIS lines across a range of temperatures ($\log[T/K] = 5.65$ to 6.30) shows that the loops are clearly discernible in the lower temperature lines and gradually fade at higher temperatures.

In order to have a clear understanding of the location of fan loop footpoints of with respect to the sunspot, in the left panel of Figure 4 we show the HMI continuum image overplotted with blue contours of fan loops obtained from AIA 171 Å. The yellow (level = 22,000) and black (levels = 55,000) contours demarcate the boundary of the umbra and penumbra of the sunspot, respectively. The middle panel shows an *IRIS*1400 Å slit-jaw image overplotted with the same contours as in the left panel. The overlying cyan box indicates the *IRIS* raster FOV (reduced along the *y*-direction). The right panel image shows an AIA 171 Å image overplotted with B-field contours of level −1200 G, demarcating the large sunspot as well as the anomalous polarity region inside the umbra. As can be inferred from the images, the fan loops are rooted well inside the umbra, exactly at the location where the sunspot shows anomalous behavior. Additionally, the footpoints appear brighter in the *IRIS* Si IV 1400 Å slit-jaw image. We have checked the HMI magnetogram data and found that the region with the anomalous magnetic field persisted over few days. So did the fan loops.

Since we are interested in quiescent AR fan loops, it is important to demonstrate that the structures do not show any significant change during the time of the observations. Therefore, we look at the light curves along the fan loops and check their stability over time. The fan loops emerging from the sunspot region in the AIA 171 Å channel and the corresponding variation of intensity along a loop for the entire duration of all six rasters of *IRIS* (∼32 minutes between 10:31:15 UT and 11:03:07 UT) shows that the maximum fluctuation in the entire period is <4%, near the apex. However, the fluctuations closer to the footpoints are smaller. Note that the fluctuations are computed as the difference of maximum and minimum intensities of the mean intensity over all the six rasters. It is emphasized that no treatment of background or foreground intensities was performed. According to López Fuentes & Klimchuk (2015), any small intensity fluctuation in loops could be attributed to a background or foreground contribution. From the temporal evolution plot as well as from visual inspection of the *IRIS* and AIA movies, we are confident that there has been no major eruptive event within this duration that could produce such foreground or background changes.

3.1. Measurement of Electron Density

Using the density-sensitive line pairs of O IV (*IRIS*) (1399.77 Å and 1401.16 Å formed at $\log[T/K] = 5.15$) and Si X (EIS) (258.37 Å and 261.04 Å formed at

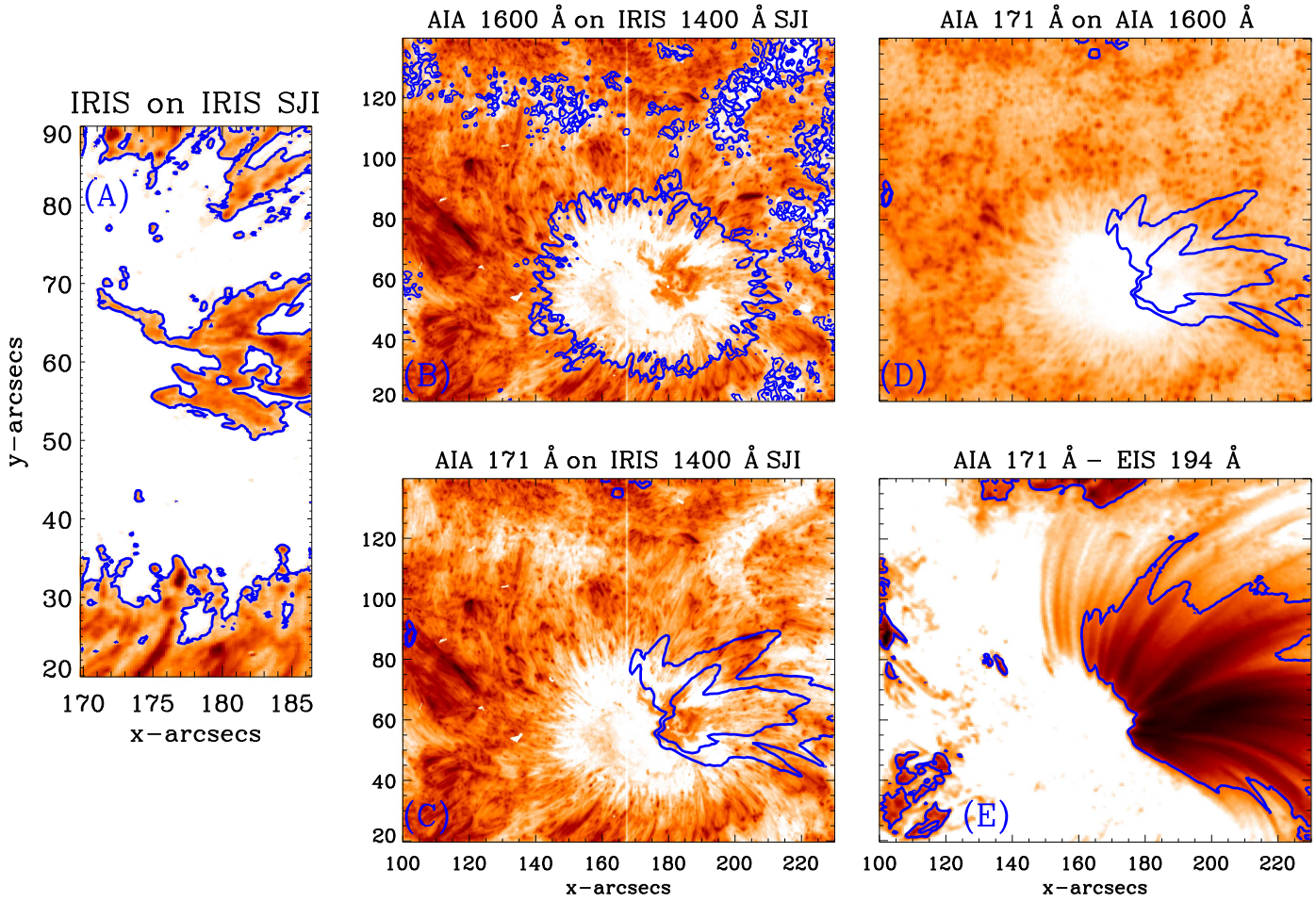

Figure 2. Coaligned images of AIA, EIS, and *IRIS* at comparable temperatures. (A): *IRIS* raster Si IV in the 1402.77 Å spectral line (contours) coaligned with *IRIS* Si IV 1400 Å SJI (background). (B): AIA 1600 Å image (contours) coaligned with *IRIS* Si IV 1400 Å SJI (background). (C): *IRIS* Si IV 1400 Å (background) slit-jaw image coaligned with AIA 171 Å (contours). (D): AIA 171 Å fan loops (contours) superimposed on AIA 1600 Å (background) with coalignment. (E): EIS Fe VIII 194.66 Å (contours) superimposed on AIA 171 Å image (background) after coalignment. The fan loop contours are clearly visible in images (C), (D), and (E). All images display negative intensities.

log $[T/K] = 6.15$), we have determined the electron densities at the footpoints and in the fan loops.

The aim is to compute the average electron density at the footpoint of fan loops, denoted by box E ($5\farcs6 \times 17\farcs84$) in all three panels of Figure 5. Figure 5 provides the two intensity maps obtained for O IV lines (left and middle panel) and the derived density map (right panel). Note that the FOV in the *y*-direction has been reduced so as to zoom into the footpoints in all the *IRIS* maps shown in the paper. Because the O IV lines are weak, fitting problems at pixels with poor counts arise. In order to improve the S/N, we binned the data by 4×4 pixels.

In order to determine the goodness of the fits, we randomly picked six small regions (e.g., A–D (at the footpoints) and F and G (away from footpoints), each being $0\farcs66 \times 0\farcs83$ as shown in Figure 5 scattered across the *IRIS* raster FOV. The fit worked very well in the footpoint regions (i.e., in regions A–D) but not in the other regions (i.e., in F and G). In addition, we calculated the average density in fan loops by considering a larger box E. The average densities obtained in the four small boxes (A–D) and the large box (E) are given in Table 2. Including the three factors that incorporate errors in the density estimation, i.e., photon count error, fitting error, and atomic data errors, we estimate that the total uncertainty in the measurement does not exceed 20% of the estimated values. On average, the density at the footpoints of the fan loops within box E is estimated to be $\log N_e \sim 10.1\,\mathrm{cm}^{-3}$. For the boxes A to E, shown in Figure 5, we also estimated the electron densities using the Si X line pair observed by EIS. Note that the data for the Si X lines were binned by 4 pixels in the *y*-direction in order to increase the S/N. The densities we obtained are also listed in Table 2.

The electron density values given in Table 2 reveal that the densities measured using Si X at $\log [T/K] = 6.15$ are lower than those measured using O IV at $\log [T/K] = 5.15$. This is suggestive of constant pressure at the footpoints of the fan loops. In addition, it also suggests that there are probably a number of coronal strands within the volume where these densities are measured. The plasma in some of these strands is at $\log [T/K] = 5.15$ and for some others it is at $\log [T/K] = 6.15$. This could be better confirmed by estimating the spectroscopic filling factor (Cargill & Klimchuk 1997), which requires the structures to be resolved, for example as in Tripathi et al. (2009) and Gupta et al. (2015). Unfortunately, the structures at the footpoints in the present study are not very well resolved, which prevented us from performing such estimates. We furthermore note that due to poor counts, the estimate of Si X densities likely suffers from a large uncertainty and may be considered as an upper limit.

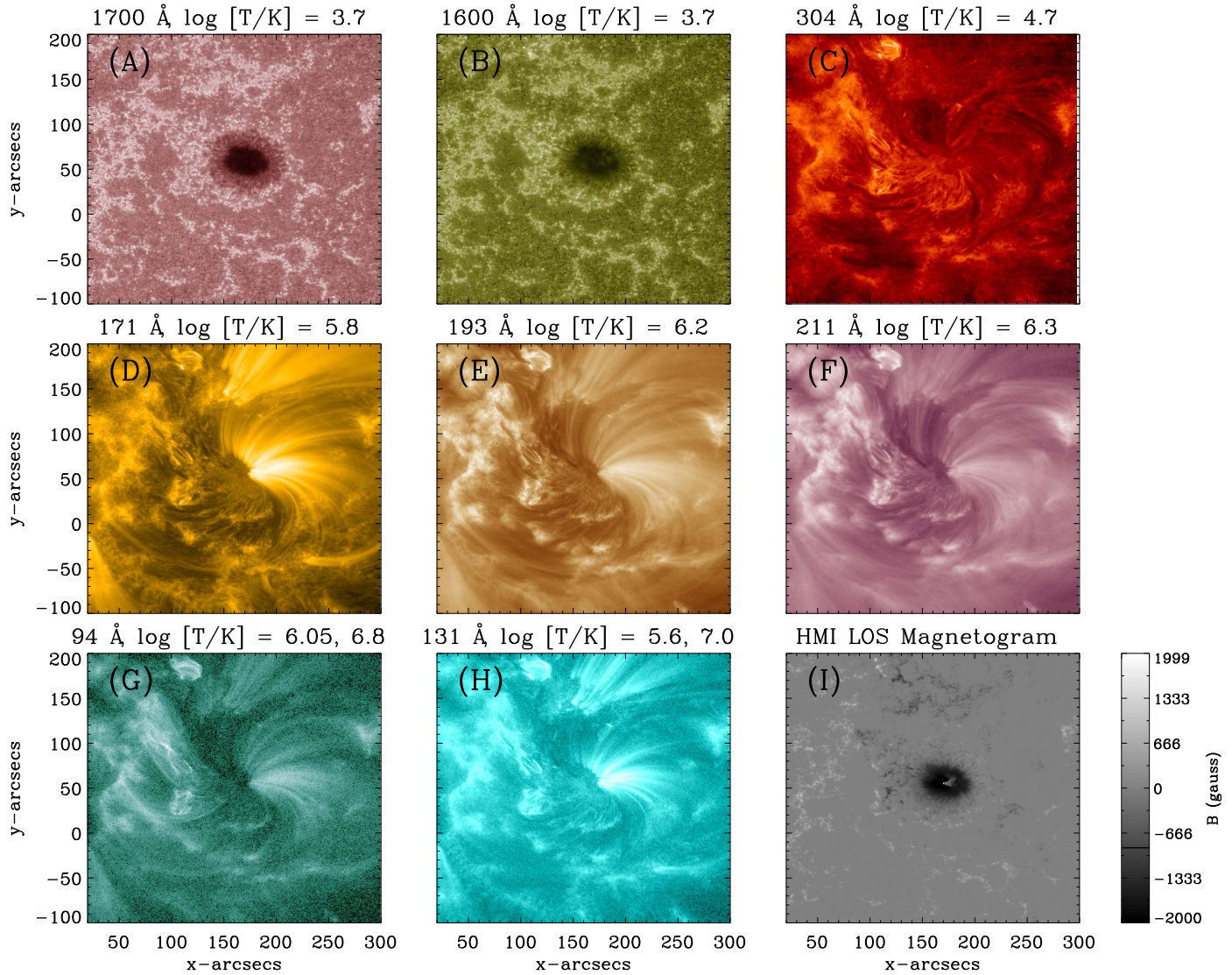

Figure 3. Images of AR 11899 on 2013 November 19 in the 8 AIA/*SDO* channels in order of increasing temperature and an HMI LOS magnetogram. The channels and their corresponding peak formation temperatures (in log scale) are also noted.

3.2. Temperature Structure of Fan Loops

Since we have fan loop observations across a range of temperatures, we have produced EM-Loci (Jordan & Wilson 1971; Del Zanna et al. 2002) plots for four loop structures (loops I, II, III, and IV as indicated in Figure 6) in order to follow the temperature structure along the loop length. Several small boxes (A–V, each $3'' \times 4''$) have been identified on these loops. The numbering with capital letters identifies the regions on the loops, while the numbering with small letters indicates the respective background or foreground. A radiometric calibration has been performed on the *IRIS* spectral data using the *IRIS* software.[11] To calculate the contribution function, we used the photospheric abundances[12] and ionization equilibrium[13] given by CHIANTI (v7.1.3) spectral synthesis package (Dere et al. 1996; Landi et al. 2013).

We have obtained the EM-Loci curves for all the four loops (Figure 6), but in Figure 7 we only show the EM-Loci plot for loop II. We emphasize here that the other loops provide very similar results. They are not shown here for brevity. The boxes far away from the footpoints have no signatures of the low-temperature lines (Si IV and O IV) observed by *IRIS*. The *IRIS* lines are available only at the first three locations (first three panels, upper row). Each panel corresponds to a pair of locations (indicated at the top of each panel). The intensity within the region denoted by the capital letter represents the loop, while the region denoted by the corresponding small letter is considered as the background or foreground. The lines to which the plotted curves correspond are labeled in the second panel of the bottom row. From Figure 7, we note that closer to the footpoints, the EM-Loci curves for the *IRIS* lines intersect at one point ($\log [T/K] \sim 4.95$) and the curves for the EIS spectral lines intersect at another point ($\log [T/K] \sim 5.95$). This difference between *IRIS* and EIS could be due to EIS and *IRIS* cross calibration. However, the difference is rather too large to be explained by merely considering cross calibration. Another possibility could be that

[11] ITN 26: A Users Guide to *IRIS* Data Retrieval, Reduction and Analysis, 2015 September.
[12] *Sun_photospheric_2011_caffau.abund.*
[13] *chianti.ioneq.*

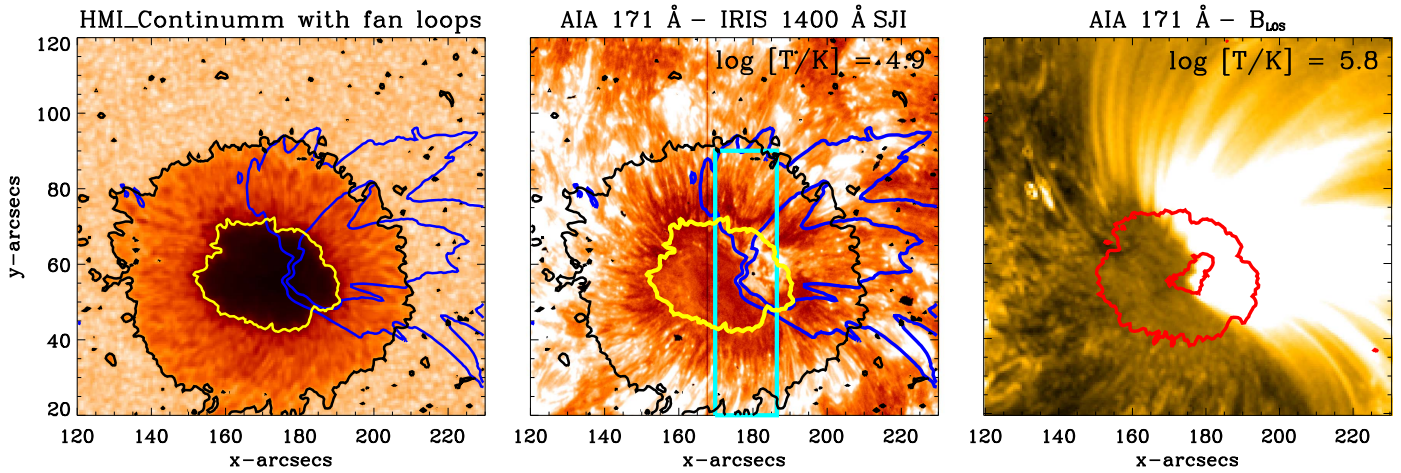

Figure 4. Left panel: the HMI continuum image with the yellow contour (level = 22,000) shows the boundary between the umbra and penumbra, the black contour (level = 55,000) demarcating the boundary between the penumbra and the quiet Sun (typically ∼62,000). The blue contours are the fan loops as seen in the AIA 171 Å channel (defined by levels between 800 to 1800, whereas the quiet-Sun region has typical values of 100–200). Middle panel: intensity map of AIA 171 Å (blue contours) overplotted on IRIS SJI Si IV 1400 Å. The superimposed cyan box denotes a portion of the *IRIS* raster image showing that the fan loops originate from the footpoint region identified with *IRIS*. The black contour denotes the sunspot penumbra (level = 55,000), whereas the yellow contour denotes the sunspot umbra (level = 22,000). Right panel: a blow-up of the AIA 171 Å channel image displaying the fan loops and where they are rooted in the sunspot umbra (denoted by the outer red contour). The inner red contour represents a region of anomalous polarity within the sunspot umbra.

the plasma in the fan loops has two temperature components—a cooler component (seen by *IRIS* lines) and another, warmer component (observed by EIS lines)—at the footpoints. Considering the fact that we have obtained two different values of the electron density at two temperatures in the previous section, the existence of two plasma components seems more likely.

At the bottom of each panel, the histograms are shown that indicate the number of crossings in each temperature bin of width $\log [T/MK] = 0.1$. We defined the formation temperature of the fan loops as the middle point of the temperature bin at which at least four such crossings are present. Following this convention, it is noted that the maximum number of lines cross within the bin $\log [T/K] = 5.90$ to 6.00 at all the six locations of loop II, i.e., the temperature of fan loops is $\log [T/K] = 5.95$, which is similar to the values obtained by Brooks et al. (2011). The errors are estimated to be one bin on either side of the bin with a maximum number of crossings. The plots also reveal that the temperature remains almost constant at $\log [T/K] \sim 5.90$ to 6.0 along the lengths of the loops. The AIA (Figure 3) and EIS intensity maps show that the loops are most prominent in the AIA 171 Å channel and in the Fe VIII and Si VII spectral lines (all of these have a peak formation temperature around $\log [T/K] = 5.80$). This supports the deduced temperatures.

3.3. Measurement of the Doppler Shift

The *IRIS* spectral data provide us with an opportunity to study the plasma flows at the footpoints of fan loops at transition region temperatures ($\log [T/K] = 4.40$ to 5.15). Here, we have obtained the intensity and velocity maps in the C II ($\log [T/K] = 4.40$), Si IV ($\log [T/K] = 4.90$) and O IV ($\log [T/K] = 5.15$) lines observed by an *IRIS* raster commencing at 10:31:15 UT. It is known that C II lines may show double-peaked profiles at certain locations (Rathore et al. 2015). Our analysis of the line profiles of C II lines at the footpoint of fan loops suggests that they could be well represented by a single Gaussian. We note here that there are two lines for C II, two for Si IV, and two for O IV, as listed in Table 1. We have derived the intensity and Doppler maps in all six lines, but show the results for one spectral line for each ion. The results for the other lines are similar.

The intensity and corresponding Doppler maps for the *IRIS* lines are shown in Figure 8. Note that the intensity maps are shown in negative colors. Since the C II and O IV lines are weak, they were binned over 4 × 4 pixels. The footpoints of the fan loops are clearly visible in Si IV as well as in O IV lines and are predominantly redshifted. The redshift is weakest in C II (∼2–3 km s^{-1}) with a peak formation temperature at $\log [T/K] = 4.40$. With increasing temperature it increases to about 10–15 km s^{-1} in Si IV ($\log [T/K] = 4.90$) and further increases to 15–20 km s^{-1} in O IV ($\log [T/K] = 5.15$). Note that the average errors in these measurements are about 3 km s^{-1}.

The footpoint region has been rastered by *IRIS* six times over a period of ∼32 minutes. This provided us with an opportunity to study the variation of Doppler shifts in *IRIS* lines as a function of time. We have chosen a region that covered the entire footpoint to study the variation of the average Doppler shift. The velocities are relatively stable with a tendency toward a decreasing strength of downflows.

4. Summary and Discussion

In this paper, we have studied the plasma parameters of fan loops (at the footpoints as well as along the loops) using observations recorded by *IRIS*, EIS, and AIA. The spectroscopic observations were used to measure the parameters (electron density, temperature, and Doppler shifts), whereas the high-cadence imaging observations provided by AIA were used to ensure that the loops did not evolve drastically during the course of the *IRIS* and EIS raster observation. In addition, AIA data were used to coalign the observations from *IRIS* and EIS.

The fan loops are observed at near-simultaneous times by AIA, EIS, and *IRIS*. The footpoints of fan loops are seen at both chromospheric and transition region temperatures

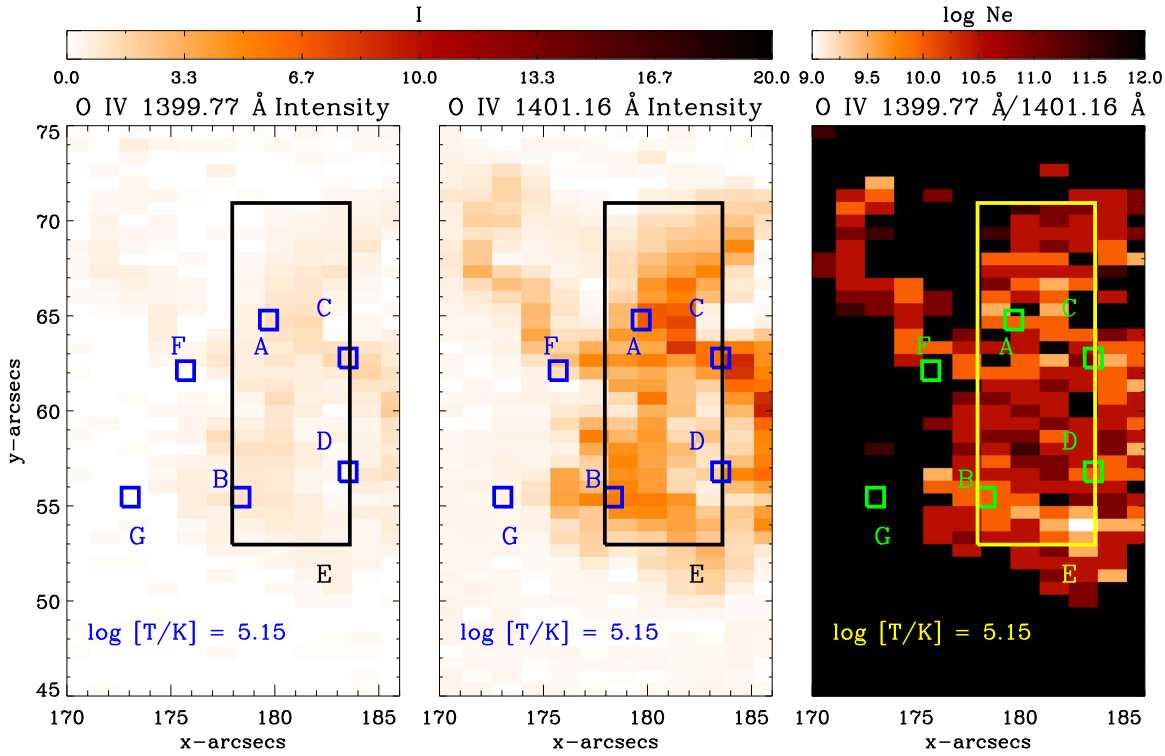

Figure 5. Intensities in the two O IV lines of *IRIS* formed at log $[T/K] = 5.15$ (left and middle panel) and density (right panel) map obtained from them. Since the O IV lines are very weak, 4×4 pixel binning has been carried out.

Table 2
Average Electron Densities in Four Small Boxes (Figure 5) within the Footpoints of Fan Loops Investigated using *IRIS* O IV and EIS Si X Line Pairs

Location	log $N_e \pm 20\%$ (O IV)	log $N_e \pm 20\%$ (Si X)
A	10.0	9.1
B	9.9	8.9
C	10.4	9.0
D	9.9	8.8
E	10.1	8.9

Note. A 20% uncertainity is acceptable in these figures.

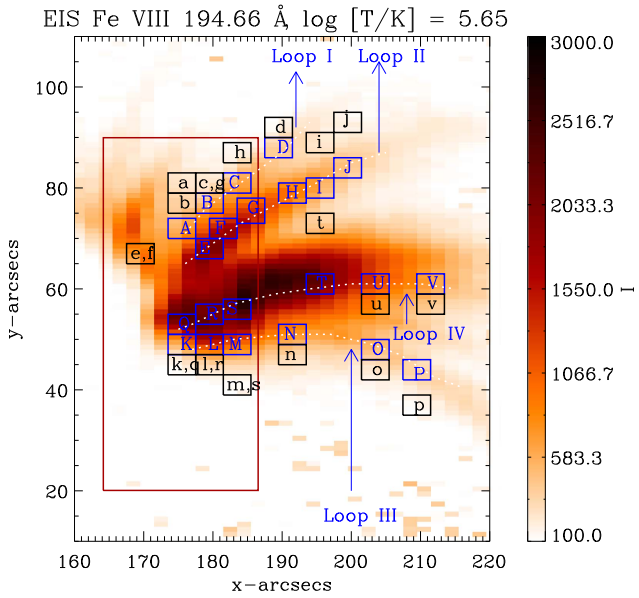

Figure 6. EIS Fe VIII 194.66 Å image showing the fan loops. Four loops (loops I, II, III, and IV) have been identified. The boxes ($3'' \times 4''$) mark the regions selected for Emission Measure studies. Capital letters are used to identify the boxes that sample the loops, while boxes indicated with small letters sample the respective backgrounds. The brown box outlines the *IRIS* raster FOV, which essentially captures the footpoints of the fan loops.

covering log $[T/K] = 4.90$ to 5.15. At upper transition region temperatures (log $[T/K] = 5.65$ and 5.80), the main body of the loops is distinctly visible. They emanate from the footpoints that are rooted inside the umbra of a sunspot and end at an unknown location far away (Figure 3). They become somewhat less discernible (more diffuse) as temperature increases, similar to warm loops (Tripathi et al. 2009; Guarrasi et al. 2010). We emphasize here that the footpoint, which is rooted inside the umbra of the sunspot, shows anomalous behavior in magnetic field measurements.

Below we summarize the main results obtained in this study.

1. Electron densities in various regions at the footpoints of the fan loops are measured using the density-sensitive line pairs of O IV (log $[T/K] = 5.15$) and Si X (log $[T/K] = 6.15$) observed with *IRIS* and EIS, respectively. The average electron density at the footpoints of fan loops is $\log N_e = 10.1$ cm^{-3} for O IV and $\log N_e = 8.9$ cm^{-3} for Si X.

2. The temperature structure in the loops (cross-field as well as along the loops) was studied using the EM-Loci of the spectral lines observed with both *IRIS* and EIS. For this purpose, various locations along four different loops were selected. The locations adjacent to the loops were considered as the background (see Figure 6). The *IRIS* lines are only visible close to the footpoints of the loops.

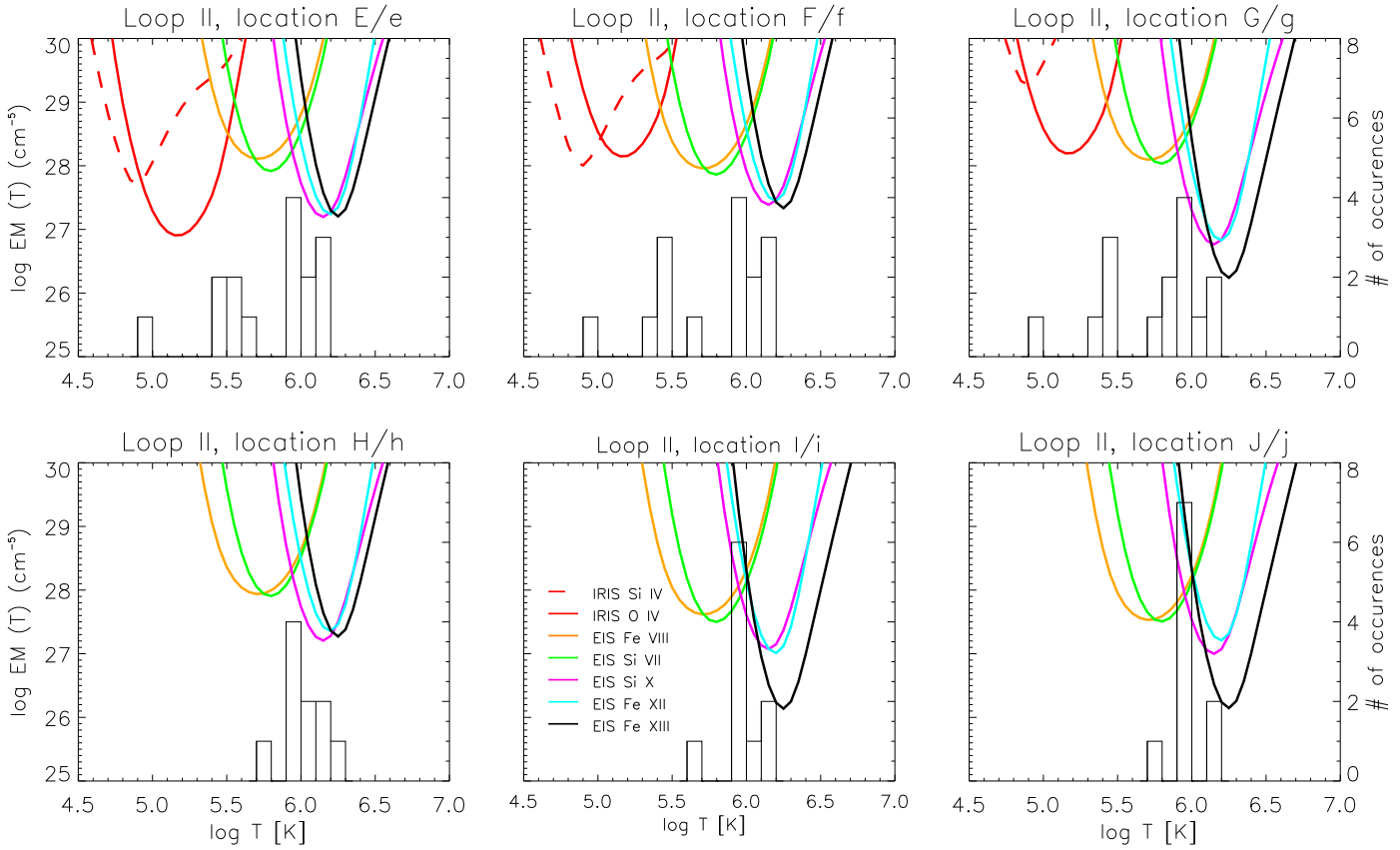

Figure 7. Emission Measure (EM) loci plots along loop II (Figure 6) using *IRIS* and EIS lines. The histograms plotted at the bottom of each panel represent that number of crossings within a temperature bin of $\log[T/MK] = 0.1$. The lines to which the plotted curves correspond are labeled in the second panel of the bottom row. The solid and dashed red lines are for the *IRIS* lines (O IV and Si IV, respectively). The solid lines of other colors denote the EIS lines as shown in the figure itself.

Based on these measurements, we find that there are two components of the plasma (at the footpoints the average temperature from *IRIS* lines is $\log[T/K] \sim 4.95$ and from EIS lines it is $\log[T/K] \sim 5.95$) and remains constant thereafter. In the upper part of the loops, the EM-Loci curves from EIS suggest that all four loops studied are mildly multithermal across the line of sight around $\log[T/K] = 5.95$.

3. The Doppler velocities of the plasma at the footpoints of fan loops are studied using spectral data from *IRIS* in C II ($\log[T/K] = 4.40$), Si IV ($\log[T/K] = 4.90$) and O IV ($\log[T/K] = 5.15$). In all these lines the plasma inside the fan loops is predominantly redshifted (downflow) by 2–3 km s^{-1}, 10–15 km s^{-1}, and 15–20 km s^{-1}, respectively, and it increases with increasing temperature within the observed temperature range. We furthermore note that the observed redshifts at the footpoints persist for a span of more than 30 minutes.

Our measurements of electron densities being higher at lower temperatures and vice versa suggest that the fan loops are at constant pressure. The measurements also suggest that the loops are comprised of several loop strands within the volume we studied. This is further verified by the temperature structure obtained using an EM-Loci analysis, which showed two-component plasmas at the footpoints, one detected in cooler lines observed by *IRIS* and the other in lines observed by EIS. The Doppler measurement also shows plasma at the temperature that is detected by the temperature analysis. Unfortunately, we did not have a good enough wavelength calibration to derive velocities at higher temperatures using EIS lines.

A comprehensive understanding of the physical parameters provides important constraints on the modeling of active region loops. In addition, the observed patterns of density, temperature, and flows can be compared with those predicted by different models. In general, two mechanisms have been proposed to explain the heating of active region loops—i.e., high-frequency nanoflares (steady heating where thermal conduction flux is eventually balanced by the radiative output), and low-frequency nanoflares (impulsive heating) where the enthalpy flux (see e.g., Bradshaw & Cargill 2010) from the corona is maintained by radiative cooling. The high- and low-frequency scenarios are defined by how frequently the heating occurs as compared to the time it takes for the loops to cool after a heating event has taken place. If this interval between two consecutive heating events is shorter than the cooling time, then it is defined as high-frequency heating, thereby allowing a minimum loss of energy between these two events (for further explanation see, e.g.,Tripathi et al. 2011). The observational signatures for high-frequency heating are narrow EM distributions (i.e., isothermal cross-field structures) and no Doppler motion unless the loops are asymmetric (Boris & Mariska 1982; Mariska & Boris 1983; Marsch et al. 2004). For low-frequency heating, the signatures are instead multithermal structures across the loops coupled with Doppler motions. However, the width of the EM curve can vary depending on the nature of

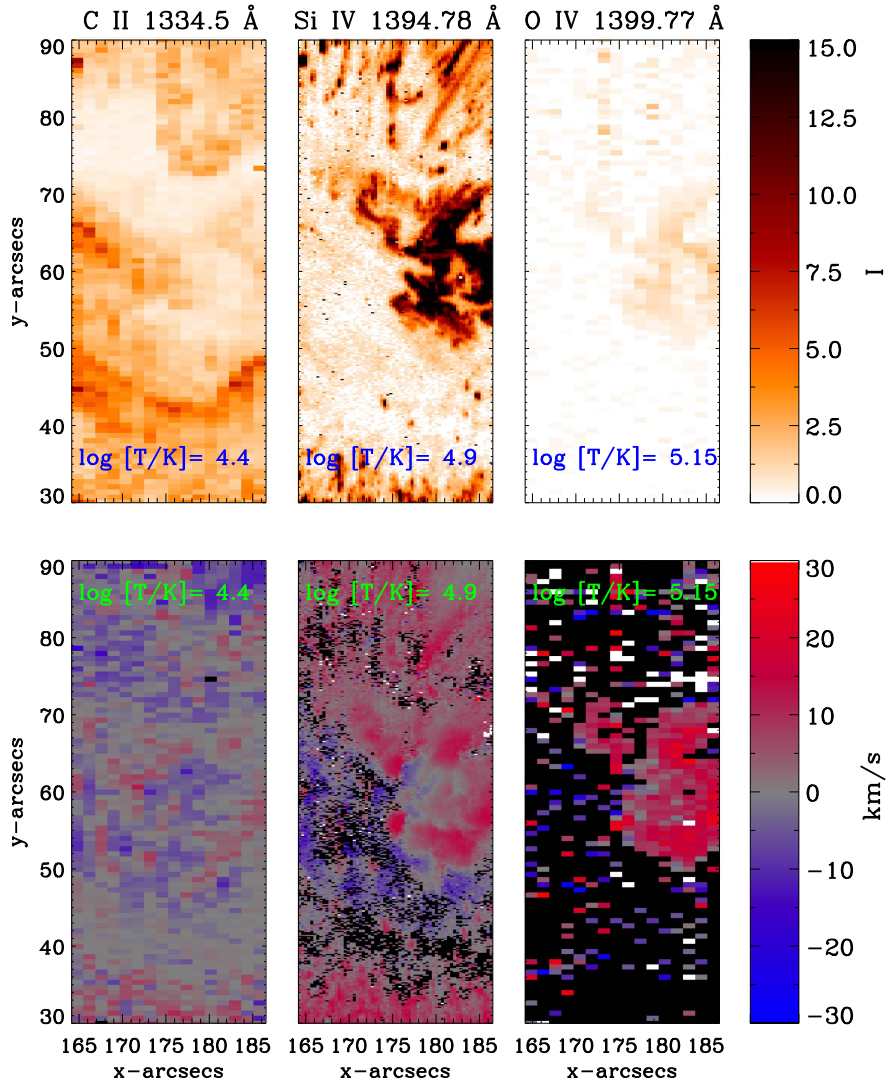

Figure 8. Monochromatic intensity (plotted as negative colors) and Doppler maps obtained in C II 1334.5 Å ($\log[T/K] = 4.40$), Si IV 1394.78 Å ($\log[T/K] = 4.90$), and O IV 1399.77 Å ($\log[T/K] = 5.15$) lines observed with *IRIS*. The images have been arranged in order of increasing temperature. The C II and O IV lines have been 4x4 pixel binned to improve the S/N.

nanoflare storms for impulsive heating (Klimchuk 2006; Cargill 2014).

At the footpoint of fan loops our observations show that the plasma is at least a two-component thermal structure. At greater heights the temperature across the loops becomes mildly multithermal. At the fan loop footpoints, the plasma is predominantly redshifted, which increases with increasing temperature within the observed temperature range ($\log[T/K] = 4.40$ to 5.15). The observed temperature structures and Doppler patterns are in agreement with the prediction from low-frequency nanoflares and point toward the interpretation that the fan loops are heated via an impulsive heating mechanism. However, this is entirely valid only if the loops are symmetric. In the case of asymmetric loops, there tend to be Doppler motions in the plasma that are due to differences in pressure, as was shown by Mariska & Boris (1983). However, the Doppler shifts introduced by such asymmetries are much smaller ($\sim$4–5 km s^{-1}) than those observed in the current study (15–20 km s^{-1}). Therefore, it is plausible to rule out that the flows we observed here are entirely due to the geometrical asymmetries.

One of the most important inferences of the impulsive heating mechanism is that the plasma experiences sufficient cooling and draining before it is reheated, implying that all the plasma that leaves the corona must pass through a range of transition region temperatures (see Cargill 1994). For a loop of constant pressure with time that experiences cooling, Cargill (1994) showed that the speed of the plasma flow in the transition region can be approximated as $V_T \sim \frac{T_T}{T_c}\frac{L}{\tau_r}$, where T_T and T_c are the transition region and coronal temperatures, respectively, L is the loop half-length, and τ_r is the radiative cooling time. For a projected loop half-length of $\sim$100 Mm (as estimated in the current study) and a typical radiative cooling time of 500–2000 s, we find that for a coronal temperature of $\log[T/K] = 5.95$ (as deduced from EM-Loci analysis), the Doppler shifts in the spectral lines of C II, Si IV, and O IV should be in the range 1.5–5.5 (observed values are 2–3) km s^{-1}, 4.5–18 (observed values are 10–15) km s^{-1}, and 8–31 (observed values are 15–20) km s^{-1}, respectively. These values are within the observed limits in the current study. More such observations and further modeling are required to reach a

firm conclusion. The results obtained here provide further constraints and inputs for modeling of active region fan loops.

We sincerely thank the referee, Peter Cargill, for his constructive comments that have improved the paper. We also thank Hardi Peter, Giulio Del Zanna, and Hui Tian for their helpful input regarding EIS and *IRIS* observations, and J.M. Borrero for discussion of HMI anomalies, respectively. A.G. is funded by the Max Planck partner group of MPS at IUCAA. D.T. acknowledges the Max Planck partner group of MPS at IUCAA. This work was also partly supported by the BK21 plus program through the National Research Foundation (NRF) funded by the Ministry of Education of Korea. G.R.G. is supported through the INSPIRE Faculty Award of the Department of Science and Technology (DST), India. H.E.M. acknowledges the support of STFC. We thank the *IRIS*, EIS, and *SDO* consortia for their open data policy. CHIANTI is a collaborative project involving the George Mason University, the University of Michigan (both USA), and the University of Cambridge (UK).

References

Antiochos, S. K., Karpen, J. T., DeLuca, E. E., Golub, L., & Hamilton, P. 2003, ApJ, 590, 547
Berger, T. E., de Pontieu, B., Fletcher, L., et al. 1999, SoPh, 190, 409
Boris, J. P., & Mariska, J. T. 1982, ApJL, 258, L49
Bradshaw, S. J., & Cargill, P. J. 2010, ApJL, 710, L39
Brooks, D. H., Warren, H. P., & Young, P. R. 2011, ApJ, 730, 85
Brosius, J. W., Davila, J. M., Thomas, R. J., et al. 1997, ApJ, 477, 969
Brown, C. M., Feldman, U., Seely, J. F., Korendyke, C. M., & Hara, H. 2008, ApJS, 176, 511
Cargill, P. J. 1994, ApJ, 422, 381
Cargill, P. J. 2014, ApJ, 784, 49
Cargill, P. J., & Klimchuk, J. A. 1997, ApJ, 478, 799
Culhane, J. L., Harra, L. K., James, A. M., et al. 2007, SoPh, 243, 19
Dadashi, N., Teriaca, L., Tripathi, D., Solanki, S. K., & Wiegelmann, T. 2012, A&A, 548, A115
Dammasch, I. E., Wilhelm, K., Curdt, W., & Hassler, D. M. 1999, A&A, 346, 285
De Moortel, I., & Browning, P. 2015, RSPTA, 373, 20140269
De Pontieu, B., Title, A. M., Lemen, J. R., et al. 2014, SoPh, 289, 2733
Del Zanna, G. 2008, A&A, 481, L49
Del Zanna, G. 2013, A&A, 555, A47
Del Zanna, G., Landini, M., & Mason, H. E. 2002, A&A, 385, 968
Del Zanna, G., & Mason, H. E. 2003, A&A, 406, 1089
Del Zanna, G., Storey, P. J., Badnell, N. R., & Mason, H. E. 2012, A&A, 541, A90
Del Zanna, G., Tripathi, D., Mason, H., Subramanian, S., & O'Dwyer, B. 2015, A&A, 573, A104
Dere, K. P., Monsignori-Fossi, B. C., Landi, E., Mason, H. E., & Young, P. R. 1996, BAAS, 28, 961
Doschek, G. A. 2006, ApJ, 649, 515
Doschek, G. A., Warren, H. P., Mariska, J. T., et al. 2008, ApJ, 686, 1362
Dudík, J., Dzifčáková, E., Karlický, M., & Kulinová, A. 2011, A&A, 529, A103
Guarrasi, M., Reale, F., & Peres, G. 2010, ApJ, 719, 576
Gupta, G. R., Tripathi, D., & Mason, H. E. 2015, ApJ, 800, 140
Handy, B. N., Acton, L. W., Kankelborg, C. C., et al. 1999, SoPh, 187, 229
Hassler, D. M., Rottman, G. J., & Orrall, F. Q. 1991, ApJ, 372, 710
Jordan, C., & Wilson, R. 1971, in Physics of the Solar Corona, ed. C. J. Macris (Dordrecht: Reidel), 219
Klimchuk, J. A. 2006, SoPh, 234, 41
Klimchuk, J. A. 2015, RSPTA, 373, 20140256
Landi, E., Young, P. R., Dere, K. P., Del Zanna, G., & Mason, H. E. 2013, ApJ, 763, 86
Lemen, J. R., Title, A. M., Akin, D. J., et al. 2012, SoPh, 275, 17
López Fuentes, M. C., & Klimchuk, J. A. 2015, BAAA, 57, 231
Mariska, J. T., & Boris, J. P. 1983, ApJ, 267, 409
Mariska, J. T., Warren, H. P., Williams, D. R., & Watanabe, T. 2008, ApJL, 681, L41
Marsch, E., Wiegelmann, T., & Xia, L. D. 2004, A&A, 428, 629
O'Dwyer, B., Del Zanna, G., Mason, H. E., Weber, M. A., & Tripathi, D. 2010, A&A, 521, A21
Pesnell, W. D., Thompson, B. J., & Chamberlin, P. C. 2012, SoPh, 275, 3
Peter, H., & Judge, P. G. 1999, ApJ, 522, 1148
Rathore, B., Carlsson, M., Leenaarts, J., & De Pontieu, B. 2015, ApJ, 811, 81
Reale, F. 2014, LRSP, 11, 4
Sandlin, G. D., Bartoe, J.-D. F., Brueckner, G. E., Tousey, R., & Vanhoosier, M. E. 1986, ApJS, 61, 801
Schou, J., Borrero, J. M., Norton, A. A., et al. 2012a, SoPh, 275, 327
Schou, J., Scherrer, P. H., Bush, R. I., et al. 2012b, SoPh, 275, 229
Schrijver, C. J., Title, A. M., Berger, T. E., et al. 1999, SoPh, 187, 261
Subramanian, S., Tripathi, D., Klimchuk, J. A., & Mason, H. E. 2014, ApJ, 795, 76
Tripathi, D., Klimchuk, J. A., & Mason, H. E. 2011, ApJ, 740, 111
Tripathi, D., Mason, H. E., Del Zanna, G., & Young, P. R. 2010, A&A, 518, A42
Tripathi, D., Mason, H. E., Dwivedi, B. N., del Zanna, G., & Young, P. R. 2009, ApJ, 694, 1256
Tripathi, D., Mason, H. E., & Klimchuk, J. A. 2012, ApJ, 753, 37
Ugarte-Urra, I., Warren, H. P., & Brooks, D. H. 2009, ApJ, 695, 642
Viall, N., & Klimchuk, J. 2011, BAAS, 43, 21.03
Warren, H. P., Brooks, D. H., & Winebarger, A. R. 2011a, ApJ, 734, 90
Warren, H. P., Ugarte-Urra, I., Young, P. R., & Stenborg, G. 2011b, ApJ, 727, 58
Warren, H. P., Winebarger, A. R., & Brooks, D. H. 2012, ApJ, 759, 141
Warren, H. P., Winebarger, A. R., & Mariska, J. T. 2003, ApJ, 593, 1174
Wilhelm, K., Curdt, W., Marsch, E., et al. 1995, SoPh, 162, 189
Winebarger, A., Tripathi, D., Mason, H. E., & Del Zanna, G. 2013, ApJ, 767, 107
Winebarger, A. R., Warren, H., van Ballegooijen, A., DeLuca, E. E., & Golub, L. 2002, ApJL, 567, L89
Young, P. R., Del Zanna, G., Mason, H. E., et al. 2007, PASJ, 59, 857
Young, P. R., O'Dwyer, B., & Mason, H. E. 2012, ApJ, 744, 14